

# AAPM/RSNA Physics Tutorial for Residents

## MR Imaging: Brief Overview and Emerging Applications<sup>1</sup>

### TEACHING POINTS

See last page

Michael A. Jacobs, PhD • Tamer S. Ibrahim, PhD • Ronald Ouwerkerk, PhD

Magnetic resonance (MR) imaging has become established as a diagnostic and research tool in many areas of medicine because of its ability to provide excellent soft-tissue delineation in different areas of interest. In addition to T1- and T2-weighted imaging, many specialized MR techniques have been designed to extract metabolic or biophysical information. Diffusion-weighted imaging gives insight into the movement of water molecules in tissue, and diffusion-tensor imaging can reveal fiber orientation in the white matter tracts. Metabolic information about the object of interest can be obtained with spectroscopy of protons, in addition to imaging of other nuclei, such as sodium. Dynamic contrast material-enhanced imaging and recently proton spectroscopy play an important role in oncologic imaging. When these techniques are combined, they can assist the physician in making a diagnosis or monitoring a treatment regimen. One of the major advantages of the different types of MR imaging is the ability of the operator to manipulate image contrast with a variety of selectable parameters that affect the kind and quality of the information provided. The elements used to obtain MR images and the factors that affect formation of an MR image include MR instrumentation, localization of the MR signal, gradients, k-space, and pulse sequences.

©RSNA, 2007

**Abbreviations:** FOV = field of view, RF = radiofrequency, SNR = signal-to-noise ratio, TE = echo time, TR = repetition time

**RadioGraphics 2007; 27:1213–1229 • Published online 10.1148/rg.274065115 • Content Codes:** **MR** **PH**

<sup>1</sup>From the Russell H. Morgan Department of Radiology and Radiological Science (M.A.J., R.O.) and Sidney Kimmel Comprehensive Cancer Center, Department of Oncology (M.A.J.), Johns Hopkins University School of Medicine, Traylor Bldg, Room 217, 712 Rutland Ave, Baltimore, MD 21205; the Departments of Radiology and Bioengineering, University of Pittsburgh, Pittsburgh, Pa (M.A.J., T.S.I.); and the School of Electrical and Computer Engineering and Bioengineering Center, University of Oklahoma, Norman, Okla (T.S.I.). From the AAPM/RSNA Physics Tutorial at the 2004 RSNA Annual Meeting. Received June 7, 2006; revision requested August 16; final revision received March 9, 2007; accepted March 9. Supported in part by grants 1R01CA100184 (M.A.J.), P50 CA103175 (M.A.J.), and 1R21CA095907-01 (R.O.) from the National Institutes of Health. All authors have no financial relationships to disclose. **Address correspondence to** M.A.J. (e-mail: [mikej@mri.jhu.edu](mailto:mikej@mri.jhu.edu)).

©RSNA, 2007

## Introduction

Magnetic resonance (MR) imaging has been well established as both a diagnostic and research tool in many areas of medicine because of its ability to provide excellent soft-tissue delineation of different areas of interest. For example, in the brain, T1- and T2-weighted MR imaging has evolved to be the standard of reference for anatomic definition. These sequences derive image contrast from the spin density in water and fat and from the MR relaxation parameters T1 and T2. Unfortunately, the water and fat spin densities yield only limited information and present difficulty in separating adipose tissue from nonadipose tissue unless fat saturation is employed. These relaxation parameters can be used in a wide variety of T1- and T2-weighted sequences to optimize contrast for specific diagnostic purposes. For example, T2 provides information about edema within the brain.

The link between the differences in T1 and T2 and the physiology of the various tissues, and, more important, the physiology of diseased tissue, is not always clear. Altering the MR image contrast with an intravascular contrast agent typically reveals physiologic changes in tissue that are relevant to disease processes. For example, contrast agents, such as gadolinium, administered to the bloodstream create more contrast in highly vascular regions and are retained in regions where the permeability of the interstitial space has changed. These types of changes in vascularity or tissue permeability occur in a variety of diseased tissues, such as malignant tumors and myocardial ischemia.

MR imaging plays an increasingly important role in radiologic imaging of different pathologic disorders, where the goal is developing radiologic imaging markers for noninvasive prediction of disease and response to treatment. For example, MR imaging used in oncologic imaging consists of anatomic T1- and T2-weighted sequences, dynamic contrast material enhancement (1,2), or MR spectroscopy in the brain (3–7), breast (8–13), and prostate (14,15). Dynamic contrast enhancement with gadolinium yields information on the vascular status of a lesion, and MR spectroscopy probes the intracellular (eg, choline, creatine) environment of tissue (16). When these sequences are combined, they can assist the physician in making a diagnosis or monitoring a treatment regimen.

One of the major advantages of the different types of MR imaging is the ability of the operator to manipulate image contrast with a variety of selectable parameters that affect the kind and quality of the information provided. Therefore, this article reviews the elements that are used to obtain MR images and the factors that affect the formation of an MR image—specifically, instrumentation, localization of the MR signal, gradients, k-space, and pulse sequences—as well as emerging applications in high-field-strength MR imaging (17–22).

## MR Instrumentation

The generation of MR images requires a sophisticated combination of electronics, radiofrequency (RF) generators, coils, and gradients that interface with a computer for communication between the different electronics. This combination of equipment allows localization, excitation, and acquisition of a specific tissue of interest and formation of a digital image. There are two groups of equipment that are combined to form the MR system. The first group is a command and control center, that is, the computer, interface, and data storage. The second group is specialized equipment that generates and receives the MR signal, that is, the magnet, gradients, and RF coils. This article gives only a brief introduction; the reader is referred to several references (23–29) and excellent textbooks (30–38) for a more detailed explanation of these topics.

## Magnets

The magnet provides the “external” magnetic field in which the patient or object is placed, and its performance requirements are usually defined in terms of field strength, stability, and homogeneity (34,39). There are three types of magnets that can be used in MR imaging: permanent, resistive, and superconducting.

**Permanent Magnets.**—Permanent magnets exploit the ferromagnetic properties of the metal used (eg, iron, nickel, or other metals). They are configured differently from resistive and superconducting magnets. Specifically, the main magnetic field ( $B_0$ ) of a permanent magnet is perpendicular to the object of interest, and early permanent magnets were very heavy (5–100 tons). However, newer versions are lighter and are sometimes used for limited clinical applications

such as open magnets. Advantages of permanent magnets are that they require no cooling or power to run and thus are cheaper than the other magnets. However, they cannot be turned off in emergencies and have less field homogeneity (34,38).

**Resistive Magnets.**—Recall that when an electric current flows through a wire, a magnetic field is induced around the wire based on the Maxwell equations; this principle is used for construction of a resistive magnet. Resistive magnets require cooling and power to operate but can be turned off and on (31–34). Their field strengths range from 0.1 T to 0.3 T, and they have the disadvantages of poor homogeneity and high electrical costs (34–36,38). Also, the object of interest lies parallel to the  $B_0$  field, and the usual application is similar to that of permanent magnets in the “open magnet” configuration.

**Superconducting Magnets.**—Superconducting magnets are based on the principle of cooling down ( $\sim 4^\circ\text{K}$ ) certain metal conductors so that there is little or no resistance; therefore, a high electric current can be used to generate high-strength magnetic fields (Maxwell equation) with no major heat disposition. However, in order to achieve small electrical resistance, expensive cooling cryogens (usually liquid helium) are used (31–34). Currently, most clinical systems use superconducting magnets with field strengths of 0.5–3 T, with most field strengths on the order of 1.5–3 T. Research magnets (clinical or experimental) can have field strengths of 4–9.4 T (17–21).

### Field Strength

The field strength of an MR system is a major determinant of the image contrast due to the energy exchange between the protons (water) and their environments. These interactions are governed by the magnetic moments of the protons, in particular the longitudinal relaxation parameter  $T_1$  (discussed later) (29,30). The time required for complete relaxation differs for different field strengths; for example, the  $T_1$  is shorter at lower field strengths and tends to increase at higher field strengths (29,30). These changes affect both the signal- and contrast-to-noise ratios of MR images (discussed later) (39–41).

The units of field strength of an MR system are tesla or gauss, with 1 T equal to 10,000 G. As discussed earlier, the range of magnetic field

strength is variable, from low (0.1–0.5 T), medium (0.5–1.0 T), or high (1.5 T) to ultrahigh (3.0 T or greater) (29,33,42). Although there have been vast technological advances in MR imaging over the past 40 years, the central principle for advancing the MR imaging technology has been based on finding ways to increase signal-to-noise ratio (SNR) (40,41) in the MR image or spectra. The most fundamental approach to boosting SNR has been to increase the field strength of the MR magnets. As a result, human MR imaging is currently performed at field strengths reaching 4 T (17), 7 T (21,43), 8 T (44,45), and 9.4 T (46).

### Shim and Gradient Coils

The localization of the MR signal depends on good local homogeneity (shim) of the magnetic field and variation (gradient) of the magnetic field in three different directions. This is accomplished by using both shim and gradient coils with the magnet. Basically, a shim or gradient coil is a device that can generate a spatially localized magnetic field within the main  $B_0$  field by using electric current. Physically, the shim and gradient coils are placed concentric to each other in the magnet and activated at specific times of the pulse sequence.

**Shim Coils.**—The quality of the received signal requires good field homogeneity and thus requires a shim of the local magnetic field, which is the  $B_0$  field along the  $z$  direction. When an object is placed in the main  $B_0$  field, it creates local susceptibility effects, and these susceptibility effects need to be corrected. Shim coils (also known as correction coils) are used to adjust or “shim”  $B_0$  magnetic field inhomogeneities and are very important for the quality of the received signal (33,34,36–38). The shim coils can be passive or active, depending on the configuration of the magnet. Passive shim coils are usually configured at the time of installation of the magnet by using metal plates within the bore or surface of the magnet. Active shim coils require electric current through special coils and provide additional “shimming” around the object of interest. Most clinical and research systems use both passive and active shims for control of the local magnetic field.

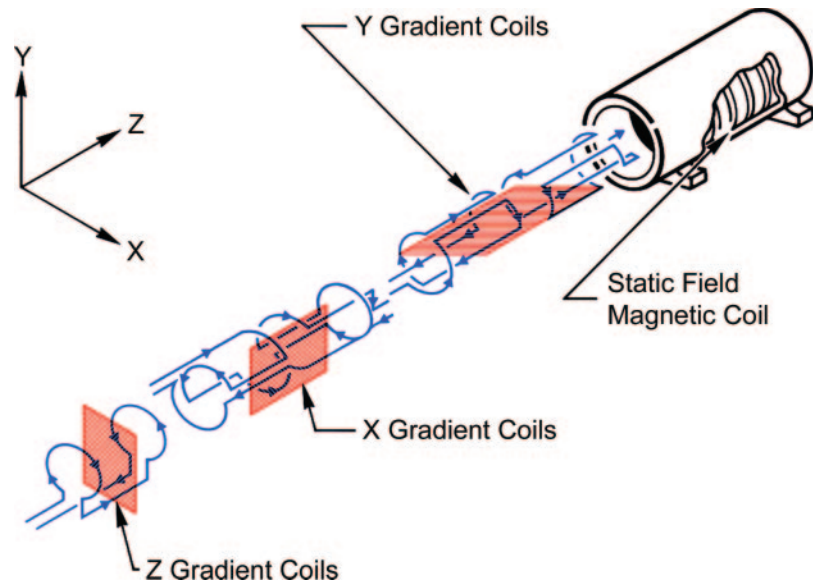


**Figure 1.** Typical gradient coil set used for localization of the MR signal. These coils are placed concentrically to each other within the magnet and are used sequentially for three-dimensional localization of the gradients to create images from the MR signal.

**Gradient Coils.**—Gradient coils are used for localization of the MR signal in three directions (x, y, and z) by using a controlled linear variation (changing) of the  $B_0$  magnetic field with distance (24,33,34,36–38). This linear variation of the magnetic field allows spatial localization of the MR signal. These coils lie concentric to each other and are used to obtain the MR images. Important parameters for gradient specification are the amplitude, rise time, and slew rate of gradient systems. The amplitude or gradient strength is defined as tesla per meter or gauss per centimeter, with  $10 \text{ mT/m} = 1 \text{ G/cm}$ . The rise time (in milliseconds) is how long it takes for the gradient system to reach its maximum strength. The slew rate of a gradient system (in tesla per meters per second) is defined as the ratio of gradient strength divided by the rise time. A typical gradient coil set is shown in Figure 1. The gradients are very important in imaging quality and image formation and are discussed further later in this article.

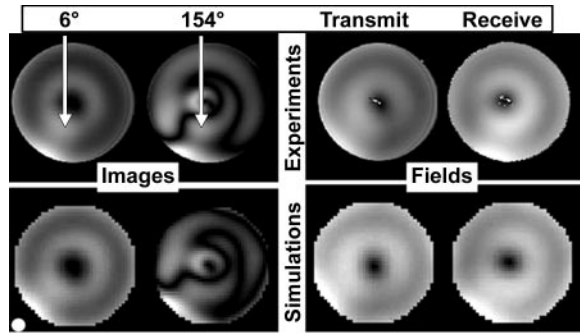
### RF Coils

The RF coils are used for two purposes: to transmit the RF energy to the tissue of interest and to receive the induced RF signal from the tissue of interest. They are placed concentric to each other and to the gradient coil system. RF coils are the “antenna” of the MR imaging system. There are

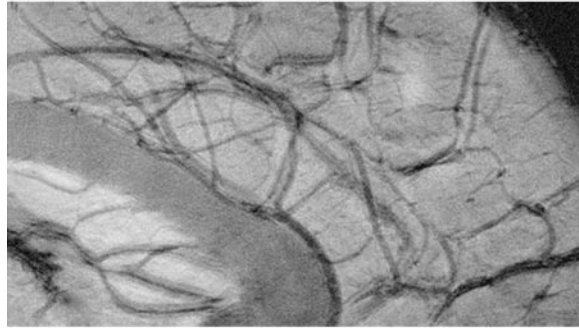
several different types of RF coils. Some are transmit or receive only or a combination of both transmit and receive. The type of coil is governed by the desired application, and the RF coil configuration can be varied; usual designs are surface, saddle, quadrature, or phased array (multiple elements). These coils can be designed for the brain, breast, or other body organs.

Therefore, the RF signal is generated by a transmit RF coil and applied to an area of interest, and the output signal is picked up by the RF receive coil and transmitted to an RF amplifier for reconstruction of the image in the main computer (23). However, with the increase in magnetic field strength ( $\sim 7 \text{ T}$ ), the principles of building RF coils will change due to the interaction of the magnetic field with the electric field as determined by the Maxwell equations (discussed later).

**Multiple RF Coils.**—So far, we have discussed the use of only single RF coils. However, use of a greater number of coil elements (or channels) has led to recent technological advances in pulse sequence design and image processing by using parallel imaging methods (simultaneous acquisition of spatial harmonics [47] or sensitivity encoding [48]). These methods have resulted in reduced imaging time but also in a decrease in SNR and are discussed later in this article.



a.



b.

**Figure 2.** (a) Low- and high-flip-angle (arrows) images and measured transmit and receive fields obtained by using an 8-T system (top row) and corresponding simulated results obtained at 340 MHz by using computational electromagnetics (bottom row) (49). (b) In vivo  $2000 \times 2000$  image of the human brain obtained at 8 T with  $100\text{-}\mu\text{m}$  resolution (20). High-field-strength magnets are increasingly being used in MR imaging research centers throughout the world.

**High-Field-Strength RF Coils and Field Distribution.**—Higher field strengths correspond to increased operational frequencies, where the wavelengths of the electromagnetic waves produced by currents on RF coils or arrays become on the order of the size of the human head or body, which will result in inhomogeneous  $B_1$  field (further subdivided into  $B_{1+}$  and  $B_{1-}$ ) distributions in biologic tissues. Both of these fields can have a devastating effect on the integrity of the images and on the safety of the patient. Demonstration of these issues is presented in Figure 2, where comparisons between experimental and simulated low- and high-flip-angle images and transmit and receive fields for a coil loaded with a head-sized sphere filled with homogeneous saline

are shown at 8 T (45). These results demonstrate the complexities and inhomogeneities of the  $B_{1+}$  and  $B_{1-}$  field distributions, which can lead to asymmetric and distinctive high-power images even though the coil, load, and excitation possess physical symmetry (45). However, high resolution within the brain can be achieved, as demonstrated in Figure 2b.

## Localization of the MR Signal

### Background

When a subject or object is placed into a magnetic field, the protons align to the main field ( $B_0$ ) in the z direction and the Larmor frequency is field dependent (eg, Larmor frequency  $\omega = \gamma B_0$ , where  $\gamma = 42.6 \text{ MHz/T}$  and is called the gyromagnetic ratio). **Localization of the MR signal is obtained by applying a gradient that produces a controlled linear spatial variation of the  $B_0$  magnetic field (z direction), which creates small perturbations to the field in three directions (x, y, and z) (Fig 1).** This linear magnetic field gradient is defined as any linear, spatial variation of the magnetic field in the z direction in any of the three directions. Usually, the gradients vary in a linear manner over the field of view (FOV) and are defined as the rate of change of the magnetic field ( $B$ ) in the direction of interest. In all, the gradients perform three functions: slice selection (z component), frequency encoding (x component), and phase encoding (y component).

Note that each gradient is generated by a separate concentric coil (Fig 1). Typical gradient system values range from 20 to 80 mT/m (1.5 T and 3 T) with increased slew rates from 30 to 220 mT/m/msec, where the slew rate is defined as the maximum gradient divided by the rise time. (The rise time is how long it takes for the gradient to go from zero to the maximum value.)

The linear dependence of the magnetic field  $B_i$  depends on the location within the magnet and is defined by the following equation:

$$B_i = B_0 + G \cdot r_i, \quad (1)$$

where  $B_i$  = the magnetic field at  $r_i$  and  $G$  is the

Teaching  
Point

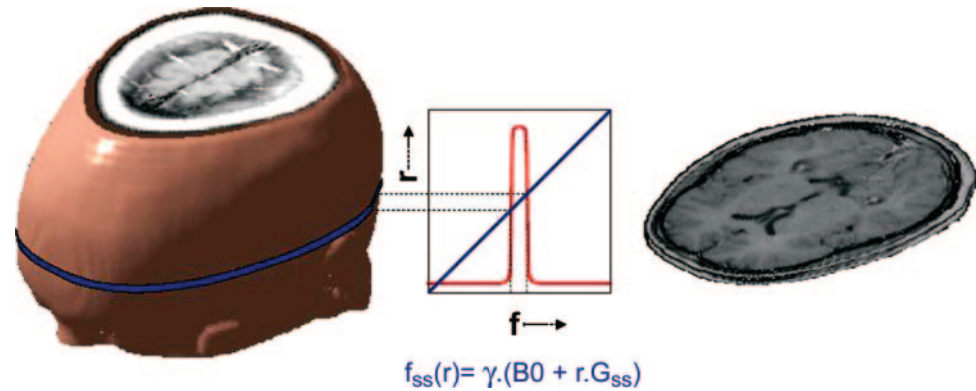


**Figure 3.** Slice selection by using the slice-selection gradient with a  $B_0$  field gradient and a frequency-selective RF pulse.

total gradient in the chosen direction. For example, the linear dependence in the x direction is as follows:

$$B_x = B_0 + G \cdot r_x. \quad (2)$$

The variation in Larmor frequency, which is the resonant frequency, caused by application of the gradient is defined by the following equation:

$$\omega_i = \omega_0 + \gamma G \cdot r_i, \quad (3)$$

where  $\omega_i$  is the Larmor frequency of interest,  $\omega_0$  is the resident frequency,  $\gamma$  is the gyromagnetic ratio,  $G$  is the gradient, and  $r_i$  is the direction. For example, application of the gradient in the x direction (usually the read direction) has the following result:

$$\omega_x = \omega_0 + \gamma G \cdot r_x. \quad (4)$$

These changes in the frequency direction are recorded for reconstruction of the image.

**Slice-Selection Gradient.**—A slice-selection gradient ( $G_z$  or  $G_{SS}$ ) determines the amount of tissue (slice) to be excited by using an RF pulse with a fixed bandwidth that is applied in the presence of a slice-selection gradient. The slice-selection gradient creates a one-to-one correspondence between the bandwidth of the RF pulse and a narrow “slice” of tissue that is to be excited. This RF pulse is called a  $B_1$  field and is applied in the presence of  $B_0$ , so that all spins (protons) are

at the same resonance frequency and the excitation is nonselective (31,37). The parameters that determine the slice thickness are the bandwidth of the RF pulse ( $\Delta f$ ) and the gradient strength across the FOV ( $G_z$ ), as shown in Figure 3. In general, larger gradients will give thinner slices and smaller gradients will give thicker slices.

**Frequency-Encoding or Readout Gradient.**—

The frequency-encoding gradient ( $G_x$  or  $G_{\text{readout}}$ ), commonly referred to as the readout gradient, is applied perpendicular to the slice-selection gradient before and during the echo formation (24). The protons are spatially “frequency encoded” by their characteristic resonant frequency along the x axis. The readout gradient is used to frequency encode the spectrum of frequencies from the object that have been created by the presence of the frequency-encoding gradient. Thus, the MR signal is always acquired during the readout gradient (Fig 4).

**Phase-Encoding Gradient.**—The phase-encoding gradient ( $G_y$  or  $G_{PE}$ ) is applied along the third perpendicular axis after the slice-selection gradient and before the readout gradient (33,34, 36,37,50,51). The phase variations occur after the initial excitation, as they begin to dephase along the applied gradient. The phase gradient induces a linear variation of the phase of the magnetization across the image (31,37). The protons will have different phase depending on where they are located; for example, usually positive phase changes occur with a higher magnetic field, whereas negative phase changes are associated with a weaker magnetic field (Fig 5). Notably,

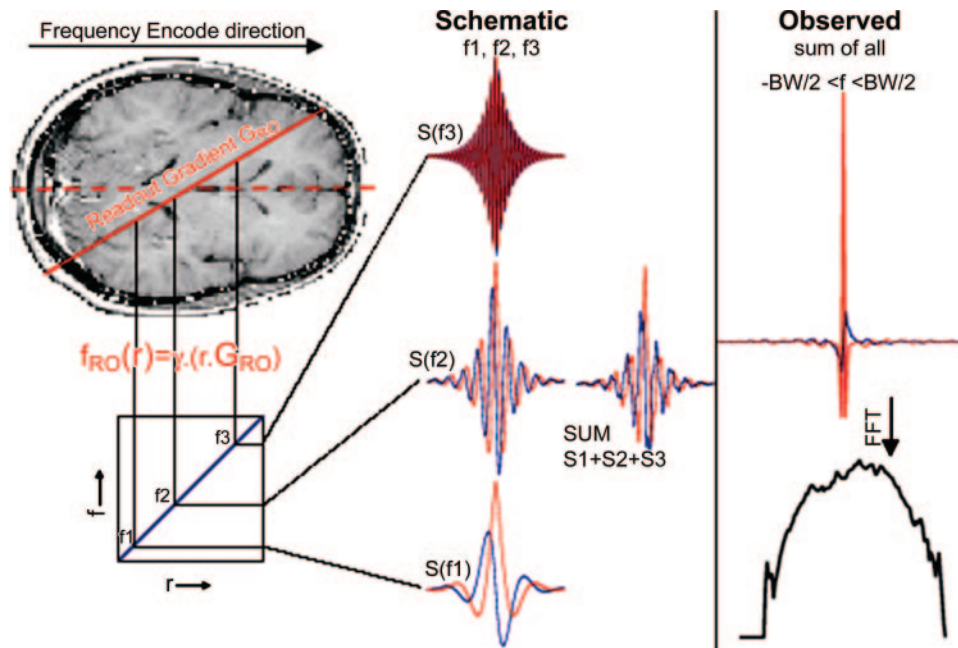


**Figure 4.** Readout gradient for three discrete frequencies associated with three positions and their summed signal. Also shown are the actual readout signal, which is the sum of signals at all frequencies within the bandwidth ( $BW$ ), and the fast Fourier transform ( $FFT$ ) of this signal, which is a projection of the object along the frequency-encoding axis.

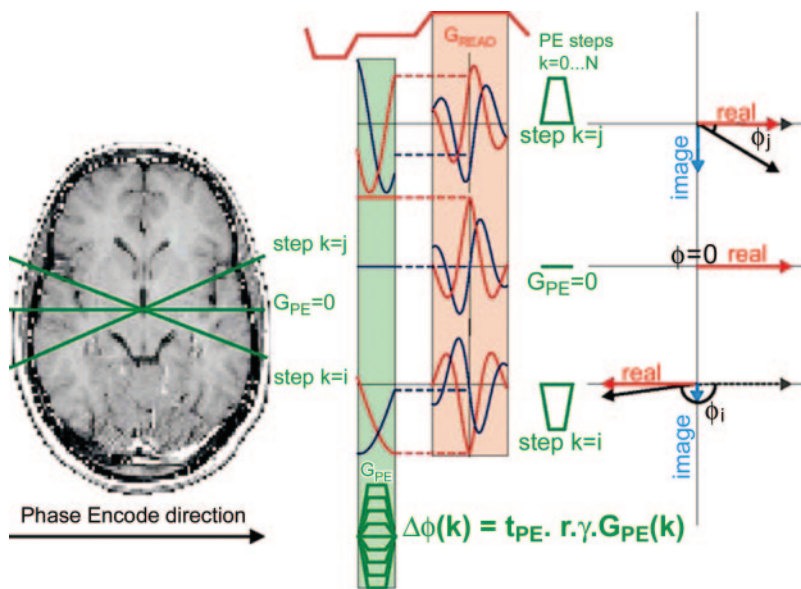


**Figure 5.** Phase encoding. The readout experiment shown in Figure 4 is repeated  $N$  times ( $N$  is the desired image resolution) with a short gradient pulse of amplitude  $G_{PE}(k)$  and length  $t_{PE}$  preceding readout. This gradient pulse temporarily changes the frequency; after period  $t_{PE}$ , the result is a phase shift  $\Delta(k, r)$ . If the gradient pulse amplitude  $G_{PE}(k)$  or length is varied in  $N$  equal steps, the resulting set of phase-encoded profiles (after the fast Fourier transform of the readout direction) will be the Fourier transform of the object along the phase-encoding direction.

most artifacts occur in the phase direction due to the longer acquisition time of the phase-encoding steps (from about 100 msec to seconds) (52).

By combining the frequency- and phase-encoding gradients, each pixel will have a distinct frequency and phase associated with it. This al-

lows creation of an image of the object by using mathematical methods. By combining all these steps into a pulse sequence, we can generate an MR image (Fig 6).

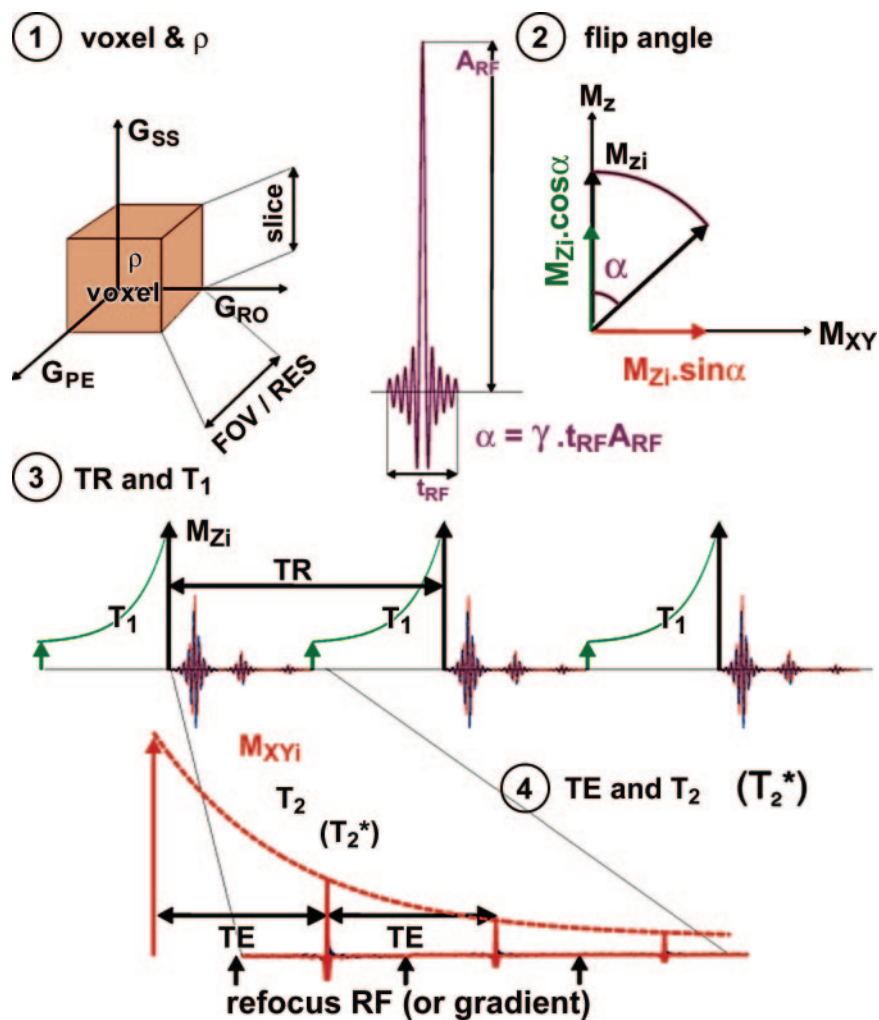


**Figure 6.** Four basic factors determining the pixel brightness of an MR image. 1, Application of each gradient for a voxel density ( $\rho$ ) for localization of the MR signal.  $RES$  = resolution. 2, Use of the RF pulse to invert the magnetization signal within the voxel ( $\rho$ ). Note that  $\alpha$  = time of the RF pulse and area covered by the pulse (eg, the strength of the pulse).  $M$  = magnetization. 3, Graphic representation of the relaxation parameter  $T_1$ .  $TR$  = repetition time. 4, Graphic representation of the relaxation parameter  $T_2$ .  $TE$  = echo time.

### MR Signal ( $T_1$ and $T_2$ )

The mechanism for contrast in an MR image is governed by the application of an RF pulse and, more important, the relaxation times of the tissue of interest, in particular  $T_1$  and  $T_2$ . After the RF pulse, an MR signal is created. This MR signal is defined by a phenomenological equation called the Bloch equation (53,54). The Bloch equation can be solved for  $T_1$  and  $T_2$  for a spin-echo sequence:

$$M(t) = M_0(1 - e^{-t/T_1}) \quad (5)$$

and

$$M_{xy}(t) = M_{xy}e^{-t/T_2}. \quad (6)$$

From these equations, we can see that MR pixel intensity is proportional to the number of protons within the tissue,  $T_1$ , and  $T_2$ . The reader should

consult the references for derivation of the Bloch equation; it is beyond the scope of this article.

$T_1$  is the longitudinal relaxation time. This occurs after application of a  $180^\circ$  RF pulse, where the magnetization vector is inverted. Then a recovery process occurs.  **$T_1$  weighting of the image is dependent on the amount of TR in milliseconds between the slice selection and RF pulses and the field strength.** For example, in a spin-echo sequence (23), the TR is the amount of time between two successive  $90^\circ$  pulses, which affects the longitudinal relaxation time. In general, fatty tissue (short  $T_1$ ) is bright on a  $T_1$ -weighted image, and water (or spinal fluid) is dark (long  $T_1$ ). Tissues that are solid have an intermediate  $T_1$  signal and may appear isointense (Fig 7).

Conversely,  $T_2$  is called the transverse relaxation time and pertains to a decay process.  **$T_2$ -weighted images are dependent on the amount of TE in milliseconds.** The TE is defined as the time of the echo. This occurs after a short waiting period ( $TE/2$ ), in which a  $180^\circ$  pulse in a spin echo is applied and an echo is formed. In contrast to  $T_1$ -weighted images, water is bright (long  $T_2$ ) on

Teaching Point

Teaching Point

Teaching Point



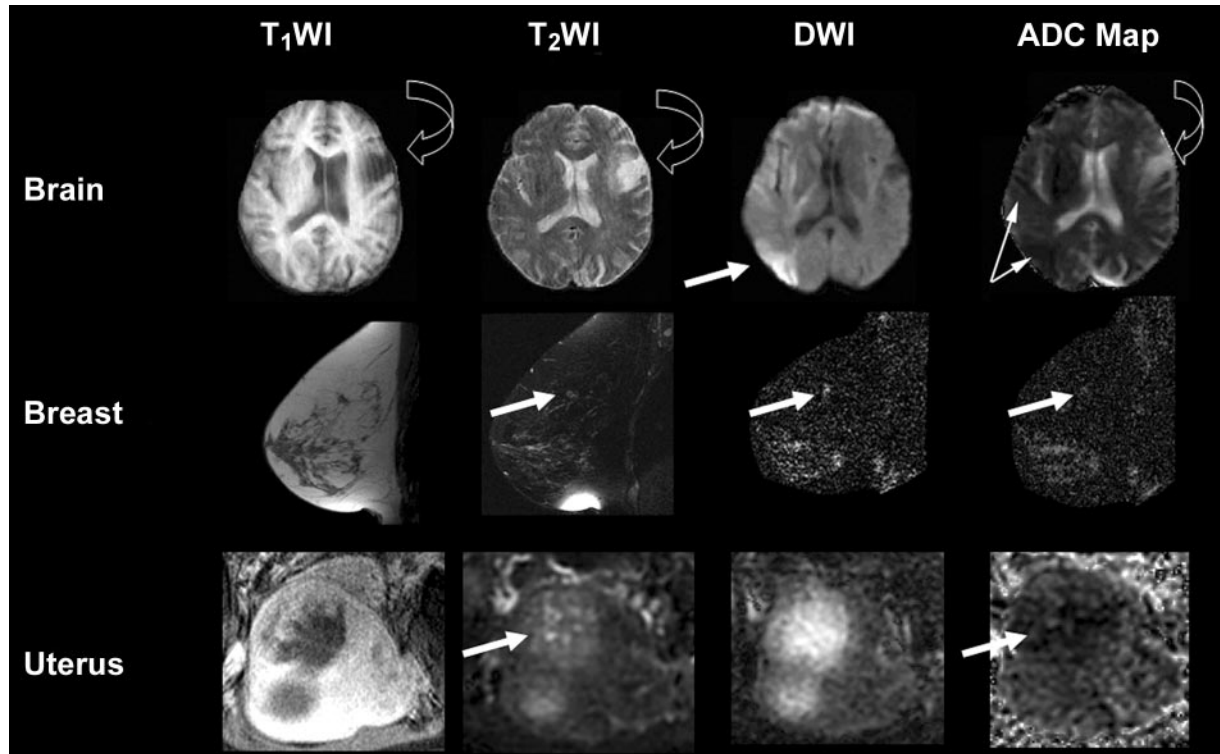


**Figure 7.** T<sub>1</sub>-weighted images (*T<sub>1</sub>WI*), T<sub>2</sub>-weighted images (*T<sub>2</sub>WI*), and diffusion-weighted images (*DWI*) from different regions of the body with corresponding maps of the apparent diffusion coefficient (*ADC*) of water. Top: Brain images of a patient with an acute stroke (<6 hours) and older infarct (>3 months). The regions of infarction are clearly visualized on the T<sub>1</sub>- and T<sub>2</sub>-weighted images as low (T<sub>1</sub>) and high (T<sub>2</sub>) signal intensity in the left temporal lobe (open arrow). Conversely, in the right occipital lobe, there is little or no change in the regions of new ischemia, except that they are seen as hyperintense areas on the diffusion-weighted image (single solid arrow). On the ADC map, there are corresponding hypointense regions (double solid arrow), which have lower ADC values. Areas that are hyperintense on the ADC map have higher ADC values. Similar signal intensities are noted on images of the breast (middle) and uterus (bottom). Note the changes (arrow in bottom row) on the diffusion-weighted image of the uterus, with decreased signal intensity in the same regions on the ADC map. Similar changes are seen on the breast images (arrow in middle row). These examples demonstrate the versatility of MR imaging in producing different image contrasts.

T<sub>2</sub>-weighted images, fatty tissue (intermediate T<sub>2</sub>) is generally isointense, and tissues that are solid have a short T<sub>2</sub> signal and may appear hypointense (depending on the TE). In terms of tissue relaxation times, T<sub>1</sub> is greater than T<sub>2</sub> for different tissues. In summary, T<sub>1</sub>-weighted images have a short TR and short TE (eg, 700/20 msec), while T<sub>2</sub>-weighted images have a long TR and long TE (eg, 2000/80 msec).

### Basic MR Sequences

There are two basic MR sequences that are frequently used for MR imaging: spin-echo or gradient-echo techniques (23,55). They differ by the number of RF pulses and the use of gradient reversals to produce an echo. Spin-echo sequences use a 90° RF pulse followed by a 180° RF pulse to generate the spin echo. Conversely, in gradient-echo methods, a single RF pulse (flip angle) is used to invert the longitudinal magnetization,

then the gradient changes from negative values and/or to positive values (gradient reversals). These gradient reversals cause phase dispersion followed by rephasing of the spins, which forms an echo (55).

### What Is k-Space?

The data obtained from the gradients (read and phase) are stored in a “matrix format” that contains all the pertinent information (eg, localization, frequency, and phase of each pixel location). In this matrix, different locations have varying amounts of signal information that is present in the reconstructed image. For example, in typical objects, high-signal information is concentrated in the center and low-signal information in general is near the peripheral sections (which define the edges). This can be demonstrated by taking

regions of the k-space out and then using mathematical transforms on the “intact” k-space to reconstruct the image (Fig 8). The matrix formation can be viewed in what is termed “k-space formalism” or “reciprocal space” (36,38,51,57, 58). Formally, k-space is defined as an array of “complex” data points ( $k_x$  and  $k_y$ ) in multidimensional space (eg, two-dimensional, three-dimensional).

We define the signal equation as follows (33,36,57):

$$s(t) \propto \int \rho(e^{-TE/T2})(1 - e^{-TR/T1}), \quad (7)$$

where  $\rho$  = proton density. Thus, we can image tissue using different tissue contrast-based applications and manipulations of the T1 and T2 characteristics. After application of each gradient (read and phase), we have a matrix of points in k-space or data space. This set of data has units of time and is sometimes referred to as the time domain.

Knowing the relationship between the FOV and gradient direction, we can relate this to the change in k-space as shown below. Recall that FOV is defined as the bandwidth divided by the gradient times the gyromagnetic ratio:

$$\text{FOV} = \frac{\text{BW}}{\gamma G}. \quad (8)$$

Now we know that the bandwidth is defined as follows:

$$\text{BW} = \frac{1}{\Delta T}, \quad (9)$$

where  $\Delta T$  is the sampling rate. Therefore, by combining the two equations, we see the following relationship:

$$\text{FOV} = \frac{\text{BW}}{\gamma G} = \frac{1}{\gamma G \Delta T}. \quad (10)$$

The units are distance (millimeters or centimeters).

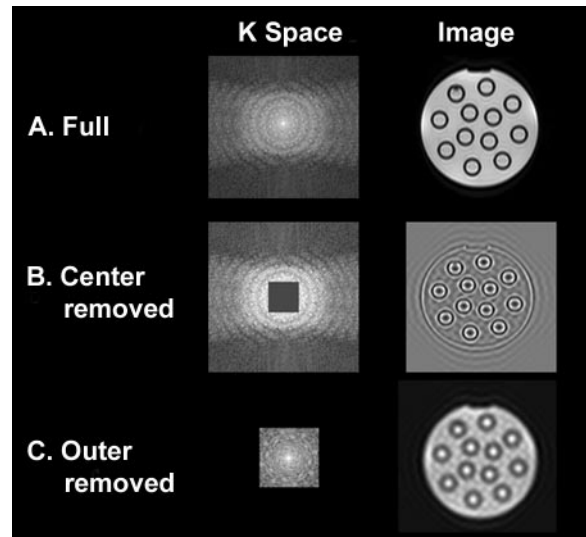


**Figure 8.** Effects of removing k-space data on a reconstructed phantom image. In *A*, image was obtained with full k-space. In *B*, image obtained with the center of k-space missing shows only edges and fine detail, which are defined by high-frequency k-space. In general, the maximum signal is obtained from the center of k-space. In *C*, image obtained with only the outer portion of central k-space removed is blurred and lacks detail. In *B* and *C*, note that removal of portions of k-space leads to ringing artifacts in the image (56).

Now we can define the following relationship:

$$\Delta k = \gamma G_i \Delta t; \quad i = x, y. \quad (11)$$

Thus, there is a direct correspondence between the FOV and gradient direction. We can relate this to the change in k-space as follows:

$$\begin{aligned} \text{FOV} = \frac{1}{\gamma G \Delta T} &\Rightarrow \gamma G \Delta T = \frac{1}{\text{FOV}} \\ &\Rightarrow \Delta k = \frac{1}{\text{FOV}}. \end{aligned} \quad (12)$$

The units of  $\Delta k$  are cycles per distance and are called the spatial frequency. Therefore, changes in the FOV are inversely proportional to the spatial frequency of k-space (38).

The traversal of k-space is dependent on the amplitude and timing of the gradients during an MR acquisition. By using mathematical operations, we can transform k-space (spatial frequency domain) into the image domain and create an image. Thus, we can define a practical use for the

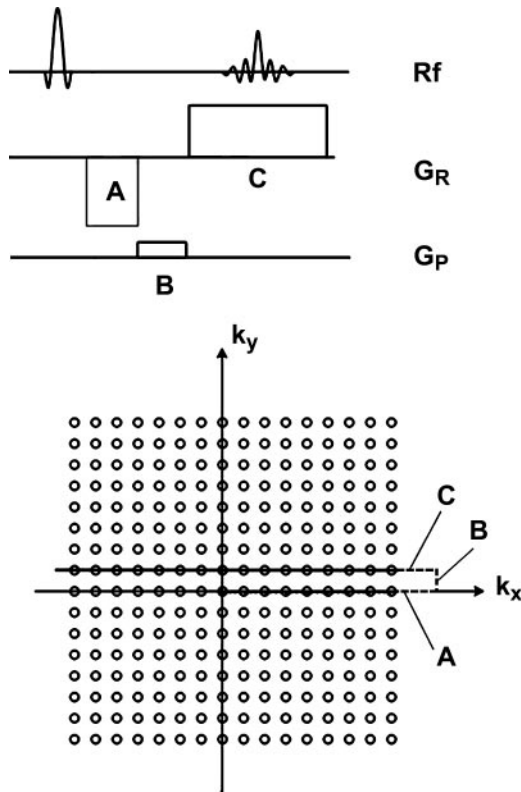


**Figure 9.** Path through k-space of a gradient-echo sequence with phase encoding. Sequence diagram shows the excitation pulse and signals RF, the readout gradient  $G_R$ , and the phase-encoding gradient  $G_P$ . The prewinding gradient  $A$  carries the k-space trajectory in the  $k_x$  direction out of the sampling area. Phase encoding with  $B$  causes an offset of the trajectory in the  $k_y$  direction, where signal from one k-line is read out under  $C$ . Data are acquired only during the last part (solid line in the trajectory), and signal during  $A$  and  $B$  is discarded (dashed line). The experiment is repeated with different  $B$  until all k-lines have been acquired (58).

k-space equation in terms of the gradients (read and phase) used in MR imaging as follows (36,38):

$$k_y = \gamma(G_{\text{phase encode}} \cdot t_{\text{phase encode}}) \quad (13)$$

and

$$k_x = \gamma(G_{\text{readout}} \cdot t_{\text{readout}}), \quad (14)$$

where  $t_{\text{phase}}$  or  $t_{\text{read}}$  is the cumulative time for each gradient (36).

Basically, for a gradient-echo sequence, after the image sequence is executed, the regions of

k-space are filled and details of certain features within the image can be visualized. The phase gradient moves the k-space vector through the trajectory from a starting point (0,0). Then, the read gradient transverses the region of k-space during the signal acquisition (eg, right to left, circular) in the  $k_x$  direction, whereas the phase gradient moves the  $k_y$ . These movements in k-space are collected into a data matrix, then a mathematical Fourier transform is applied to the data matrix to form an image (Fig 9) (31,57). Because of this knowledge, k-space acquisitions can be tailored for quicker acquisition by relying on the periodic nature of k-space, such as partial k-space acquisitions. These regions in k-space have specific properties: for example, in the typical object, the center of k-space determines much of the contrast in the image, whereas the outer regions of k-space determine capacity to image sharp edges and determine image resolution. By removing portions of the data, changes in the image can be seen (Fig 8).

This type of information is useful when looking for artifacts. Artifacts are caused by changes in the phase of the signal during the phase-encoding gradient (57,58), typically seen in areas of flow, motion,  $B_0$  inhomogeneities, and chemical shift of protons (eg, fat and water). More detailed information about k-space can be found in references 38, 51, 57, and 58.

### Parallel Imaging

Parallel imaging is a relatively new area of MR imaging and is quickly becoming a routinely used tool for decreasing imaging times in the clinical setting (59). Parallel imaging methods are based on the deployment of several RF coils (phased array) to “speed up” the acquisition of the MR signal, that is, to reduce the number of phase-encoding steps, because the imaging time required for each acquisition is proportional to the number of phase-encoding steps. The acceleration or reduction factor is called  $R$  and is usually set at 2 or 3, but this also reduces the FOV in the phase direction and leads to aliasing of the object, which is corrected by using  $B_1$  coil sensitivity maps. This concept was suggested by Hutchinson and Raff (60) and later by other investigators (61,62).

Sodickson and Manning (47) introduced parallel imaging into practice by using simultaneous acquisition of spatial harmonics (SMASH). Briefly, SMASH acquires a reduced set (determined by the  $R$  factor) of phase encodes in  $k$ -space. The  $R$  factor is defined as increasing the distance between lines of  $k_y$  with the spatial resolution at a fixed number. This leads to a reduction in imaging time.  $R$  is also known as the acceleration factor, and typical factors used are 2–3. But, with a reduction in the number of phase-encoding lines, there is a decrease in the FOV, which leads to “wraparound” or aliasing of the object. Then,  $B_1$  coil sensitivity profiles are generated and basis sets are used to approximate the missing phase-encoding lines before application of the Fourier transform to obtain an unaliased image. This requires linear combinations of  $B_1$  coil sensitivity profiles to obtain the spatial harmonics.

In contrast, Pruessmann et al (48) introduced sensitivity encoding (SENSE) as an alternative approach for SMASH parallel imaging. In SENSE imaging, the  $B_1$  sensitivity profiles of each coil are used to “unwrap” the image after the Fourier transform, and this is performed in the image domain. However, there is an SNR cost with the reduction of imaging time, that is, lower SNR in the image. In SENSE imaging, this reduction of SNR is about the square root of  $R$  and is called the geometry factor,  $g$ , which represents the noise magnification after unwrapping (37,48).

The reader is referred to the references for more in-depth detail about each method (37, 47,48). Applications of these methods are currently increasing due to improved and greater numbers of channels in the RF coils (63). This will lead to a reduction of imaging time (37) and reduced artifacts in echo-planar imaging (64) and is an active area of research.

### Contrast Mechanisms and MR Imaging Parameters

The contrast between different tissues in the MR image is defined by a complex interaction between several user-defined and tissue-of-interest variables; these are commonly referred to as intrinsic and extrinsic variables (29,33,34,36,39). The SNR is a major determinant of whether there is sufficient signal to differentiate between different tissue types. SNRs are calculated by using the following equation:

$$\text{SNR} \propto (\text{volume}) \sqrt{\frac{\#PE \cdot \text{NEX}}{\text{BW}}}, \quad (15)$$

where PE is the number of phase-encoding steps, NEX is the number of signals acquired, and BW is the bandwidth (29,39,65,66).

The signal intensity depends on several parameters that are basic to any MR sequence. For example, some MR parameters are TE, TR, flip angle ( $\alpha$ )—the angle to rotate (or tip) the magnetization vector from the main  $B_0$  field onto the transverse plane ( $5^\circ$ – $90^\circ$ )—slice thickness, and FOV (33,34,36). The amount of TR and TE determines the amount of T1 or T2 weighting for the images, respectively, whereas the slice thickness governs the amount of protons available in the tissue to image; for example, larger slices have better SNR than thinner slices but have increased partial volume effects (33,34,36). For instance, in spin-echo sequences, T1-weighted images usually have short TR (to maximize T1 differences in tissue) and short TE (to minimize T2 effects), whereas T2-weighted sequences have long TR (1500 msec) and TE (>80 msec). Therefore, the investigator can change the MR parameters (eg, TR, TE) as needed for the desired application (29,39).

### Selected Applications

The real power of MR imaging lies in the wide range of applications for which it can be used. Current applications include soft-tissue delineation, determining extent of disease, tumor staging, functional and metabolic information, and monitoring response to treatment. Some of these newer applications are outlined herein.

Teaching Point

### T1- and T2-weighted Imaging

T1- and T2-weighted imaging are the most widely used sequences for soft-tissue delineation of anatomic structures and related pathologic conditions (Fig 7). For example, in the brain, T2- and T1-weighted imaging with or without contrast material can be used to see changes in white or gray matter. In other body organs, such as the breast, extremities, and liver, and in uterine lesions, imaging has been performed by using combinations of modalities such as ultrasonography and/or T2- and T1-weighted MR imaging.

### Diffusion-weighted and Perfusion-weighted Imaging

Diffusion-weighted imaging (DWI) and perfusion-weighted imaging (PWI) are used in neurologic applications, such as brain tumor imaging (67–69) and cerebral ischemia (70–72). The use of perfusion and diffusion MR imaging techniques can identify regions of abnormal brain tissue after cerebral ischemia. PWI readily depicts areas of brain with a compromised cerebral blood

flow, whereas DWI can depict regions of ischemic tissue that may or may not recover, depending on the duration of reduced blood flow (73,74). By combining PWI and DWI methods, three scenarios can be observed:  $PWI > DWI$  (mismatch),  $PWI = DWI$  (match), or  $DWI > PWI$  (reverse mismatch) (75). For example, if PWI is larger than DWI, then the area depicted may represent “at risk” or penumbral tissue (76–78). Evaluation of these tissue characteristics is important for the targeting of therapeutic measures to maximize clinical outcomes.

DWI has been used in other organs of the body, for example, in the liver for demonstration of metastatic disease and response to treatment (79), in the uterus for monitoring treatment response from interventional procedures such as uterine arterial embolization (80) and high-intensity focused ultrasound surgery (81), and for classification of breast lesions (82). Still larger studies are needed to fully understand the impact that DWI will have in these applications.

### Spectroscopy

Proton spectroscopy has been used primarily for brain applications and recently for other organs, such as the liver, breast, prostate, and soft tissue. The use of spectroscopy expands the repertoire of clinical information by providing information on intracellular metabolites, such as choline (3.2 ppm), creatine (3.0 ppm), citrate (2.6 ppm), *N*-acetyl aspartate (2.02 ppm), and lactate (1.4 ppm) (6,7,83–85). (The unit “ppm” is defined as “parts per million” and is independent of the strength of the imaging unit.)

These metabolites are known to change in different pathologic conditions; for example, in brain tumors, *N*-acetyl aspartate (2.02 ppm) decreases with a subsequent increase in choline (6,7,85). In the breast, the presence of a choline peak (3.2 ppm) is suggestive of malignancy (11,12,86,87). In the prostate, MR spectroscopy is being increasingly used in conjunction with MR imaging to provide information on the presence or absence of citrate (2.6 ppm) and/or choline (3.2 ppm) (14,88). These applications will become routine procedures in the near future (89).

### <sup>23</sup>Na (Sodium) MR Imaging

Sodium is abundant in most tissues and is actively pumped out of healthy cells by the  $Na^+/H^+$ -ATPase pump, which maintains a large concentration difference across the cell membrane at the cost of energy-rich adenosine triphosphate. Thus, an increase in intracellular sodium concentration can be a good indicator of compromised cellular membrane integrity or impaired energy

metabolism. In the presence of tissue perfusion, the intracellular changes and concurrent increase in vascular or interstitial volume appear to be an equally good indicator of cellular membrane integrity and energy metabolism.

The intracellular sodium cannot be imaged separately from the extracellular sodium concentration without toxic shift reagents or special MR methods that cause a significant reduction in SNR and resolution (90,91). However, the total sodium concentration in tissue can be resolved by using MR imaging, and there has been increased interest in the application of sodium MR (92–98). In particular, sodium imaging has been performed in the brain (93,99), breast (95,98), heart (100), kidney (101), and uterus (102). In recent reports, sodium MR imaging has shown promise in monitoring therapeutic response (96,97,103).

### Beyond 3 T: Emerging High-Field-Strength MR Imaging (7 T and Greater)

Although there have been vast technological advances in MR imaging over the past 40 years, the central principle for advancing MR imaging technology has been based on finding ways to increase SNR (40,41) in the MR image. The most fundamental approach to increasing SNR has been to increase the field strength of the MR imaging magnets. As a result, the impetus for improved MR imaging has driven progressive increases in its magnetic field strengths from fractions of a tesla to fields of 1.5 T in the 1980s then to fields of 3 T by the mid-1990s. The next push for increasing MR imaging field strength was possible with the advancement of superconducting technology (104–106). In the late 1990s and early 2000s, the development of a human MR imaging unit above 4.1 T (17), in this case 8 T (44,107, 108), was achieved.

As a result of its tremendous potential (see Fig 2b), human MR imaging is currently performed at field strengths reaching 7 T (21,43), 8 T (44,107,108), and 9.4 T (46). The three major MR imaging vendors—GE Healthcare, Siemens Medical Solutions, and Philips Medical Systems—are developing 7-T whole-body human imaging units. However, as with many scientific breakthroughs, the potential of ultrahigh-field-strength imaging can be achieved only if other challenges are overcome. The most significant of these challenges include (a) safety concerns regarding exceeding RF power deposition (109, 110) in tissue and (b) noninherent inhomogeneity of MR imaging signal detection across the human head (22,49,108,111–113).

## Conclusions

MR imaging provides a powerful tool for diagnosis and excellent soft-tissue contrast because the image contrast can be finely optimized for specific clinical questions. Moreover, novel pulse sequence techniques allow image contrast to be based on tissue physiology or even cellular metabolism in a noninvasive manner. In addition, with ever-increasing improvement in both hardware and software, MR imaging may one day be used for screening of different pathologic conditions and provide a window into cellular metabolism and tissue physiology.

**Acknowledgments:** We thank the reviewers for their excellent comments and suggestions for this article and Mahadevappa Mahesh, MS, PhD, for his contribution.

## References

1. Evelhoch JL. Key factors in the acquisition of contrast kinetic data for oncology. *J Magn Reson Imaging* 1999;10(3):254–259.
2. Engelbrecht MR, Huisman HJ, Laheij RJ, et al. Discrimination of prostate cancer from normal peripheral zone and central gland tissue by using dynamic contrast-enhanced MR imaging. *Radiology* 2003;229(1):248–254.
3. Felix R, Schorner W, Laniado M, et al. Brain tumors: MR imaging with gadolinium-DTPA. *Radiology* 1985;156(3):681–688.
4. Nelson SJ, Huhn S, Vigneron DB, et al. Volume MRI and MRSI techniques for the quantitation of treatment response in brain tumors: presentation of a detailed case study. *J Magn Reson Imaging* 1997;7(6):1146–1152.
5. Nelson SJ. Analysis of volume MRI and MR spectroscopic imaging data for the evaluation of patients with brain tumors. *Magn Reson Med* 2001;46(2):228–239.
6. Pouwels PJ, Frahm J. Regional metabolite concentrations in human brain as determined by quantitative localized proton MRS. *Magn Reson Med* 1998;39(1):53–60.
7. Ross B, Michaelis T. Clinical applications of magnetic resonance spectroscopy. *Magn Reson Q* 1994;10(4):191–247.
8. Heywang SH, Hahn D, Schmidt H, et al. MR imaging of the breast using gadolinium-DTPA. *J Comput Assist Tomogr* 1986;10(2):199–204.
9. Kaiser WA, Zeitler E. MR imaging of the breast: fast imaging sequences with and without Gd-DTPA—preliminary observations. *Radiology* 1989;170(3 pt 1):681–686.
10. Kuhl CK, Mielsch P, Klaschik S, et al. Dynamic breast MR imaging: are signal intensity time course data useful for differential diagnosis of enhancing lesions? *Radiology* 1999;211(1):101–110.
11. Roebuck JR, Cecil KM, Schnall MD, Lenkinski RE. Human breast lesions: characterization with proton MR spectroscopy. *Radiology* 1998;209(1):269–275.
12. Jacobs MA, Barker PB, Bottomley PA, Bhujwala Z, Bluemke DB. Proton MR spectroscopic imaging of human breast cancer: a preliminary study. *J Magn Reson Imaging* 2004;19(1):68–75.
13. Macura KJ, Ouwerkerk R, Jacobs MA, Bluemke DA. Patterns of enhancement on breast MR images: interpretation and imaging pitfalls. *RadioGraphics* 2006;26(6):1719–1734; quiz 1719.
14. Kurhanewicz J, Vigneron DB, Hricak H, Narayan P, Carroll P, Nelson SJ. Three-dimensional H-1 MR spectroscopic imaging of the in situ human prostate with high (0.24–0.7-cm<sup>3</sup>) spatial resolution. *Radiology* 1996;198(3):795–805.
15. Narayan P, Kurhanewicz J. Magnetic resonance spectroscopy in prostate disease: diagnostic possibilities and future developments. *Prostate Suppl* 1992;4:43–50.
16. Gillies RJ, Bhujwala ZM, Evelhoch J, et al. Applications of magnetic resonance in model systems: tumor biology and physiology. *Neoplasia* 2000;2:139–151.
17. Bomsdorf H, Helzel T, Kunz D, Roschmann P, Tschendel O, Wieland J. Spectroscopy and imaging with a 4 tesla whole-body MR system. *NMR Biomed* 1988;1(3):151–158.
18. Roschmann P. Radiofrequency penetration and absorption in the human body: limitations to high-field whole-body nuclear magnetic resonance imaging. *Med Phys* 1987;14(6):922–931.
19. Adler DD, Wahl RL. New methods for imaging the breast: techniques, findings, and potential. *AJR Am J Roentgenol* 1995;164(1):19–30.
20. Robitaille PM, Abduljalil AM, Kangarlu A. Ultra high resolution imaging of the human head at 8 tesla: 2K × 2K for Y2K. *J Comput Assist Tomogr* 2000;24(1):2–8.
21. Wald LL, Wiggins GC, Potthast A, Wiggins CJ, Triantafyllou C. Design considerations and coil comparisons for 7 T brain imaging. *Appl Magn Reson* 2005;29(1):19–37.
22. Ibrahim TS, Abraham R, Abraham D, Tang L. RF systems for high-field MRI: problems and possible solutions based on computational electromagnetics. Meeting of the Institute of Electrical and Electronics Engineers, San Francisco, Calif, 2006; 5–8.
23. Hahn EL. Spin echoes. *Phys Rev* 1950;80(4):580.
24. Lauterbur PC. Image formation by induced local interactions: examples employing nuclear magnetic resonance. *Nature* 1973;242:190–191.
25. Mansfield P. Multi-planar image formation using NMR spin echoes. *J Phys C Solid State* 1977;10:L55–L58.
26. Bottomley PA, Andrew ER. RF magnetic field penetration, phase shift and power dissipation in biological tissue: implications for NMR imaging. *Phys Med Biol* 1978;23(4):630–643.
27. Mansfield P, Morris P; Waugh J, ed. *NMR imaging in biomedicine*. Cambridge, Mass: Academic Press, 1982.
28. Bottomley PA, Hart HR, Edelstein WA, et al. NMR imaging/spectroscopy system to study both anatomy and metabolism. *Lancet* 1983;2(8344):273–274.

29. Bottomley PA, Foster TH, Argersinger RE, Pfeifer LM. A review of normal tissue hydrogen NMR relaxation times and relaxation mechanisms from 1–100 MHz: dependence on tissue type, NMR frequency, temperature, species, excision, and age. *Med Phys* 1984;11(4):425–448.
30. Slichter C. Principles of magnetic resonance. New York, NY: Springer-Verlag, 1990.
31. Nishimura DG. Principles of magnetic resonance imaging [the white book]. D. G. Nishimura, 1996.
32. Vlaardingerbroek M, den Boer J. Magnetic resonance imaging. Berlin, Germany: Springer-Verlag Telos, 1999.
33. Haacke M, Brown R, Thompson M, Venkatesan R. Magnetic resonance imaging: physical principles and sequence design. New York, NY: Wiley-Liss, 1999.
34. Bushberg J, Seibert A, Leidholdt E, Boone J. Essential physics of medical imaging. Philadelphia, Pa: Lippincott Williams & Wilkins, 2002.
35. Hendee WR, Ritenour ER. Medical imaging physics. New York, NY: Wiley-Liss, 2002.
36. Brown MA, Semelka RC. MRI: basic principles and applications. 3rd ed. New York, NY: Wiley-Liss, 2003.
37. Bernstein MA, King KF, Zhou XJ. Handbook of MRI pulse sequences. Burlington, Mass: Elsevier Academic Press, 2004.
38. Hashemi RH, Bradley WG, Lisanti CJ. MRI: the basics. Philadelphia, Pa: Lippincott Williams & Wilkins, 2004.
39. Edelstein WA, Bottomley PA, Hart HR, Smith LS. Signal, noise, and contrast in nuclear magnetic resonance (NMR) imaging. *J Comput Assist Tomogr* 1983;7(3):391–401.
40. Hoult DI, Lauterbur PC. The sensitivity of the zeugmatographic experiment involving human samples. *J Magn Reson* 1979;34(2):425–433.
41. Hoult DI, Richards RE. The signal-to-noise ratio of the nuclear magnetic resonance experiment. *J Magn Reson* 1976;24(1):71–85.
42. Gillies R. NMR in physiology and biomedicine. New York, NY: Academic Press, 1994.
43. Vaughan JT, Garwood M, Collins CM, et al. 7T vs. 4T: RF power, homogeneity, and signal-to-noise comparison in head images. *Magn Reson Med* 2001;46(1):24–30.
44. Robitaille PM, Abduljalil AM, Kangarlu A, et al. Human magnetic resonance imaging at 8 T. *NMR Biomed* 1998;11(6):263–265.
45. Ibrahim TS, Kangarlu A, Chakeres DW. Design and performance issues of RF coils utilized in ultra high field MRI: experimental and numerical evaluations. *IEEE Trans Biomed Eng* 2005; 52(7):1278–1284.
46. Vaughan JT. How to do RF at high fields. Presented at the annual meeting of the International Society for Magnetic Resonance in Medicine, Miami, Fla, 2005.
47. Sodickson DK, Manning WJ. Simultaneous acquisition of spatial harmonics (SMASH): fast imaging with radiofrequency coil arrays. *Magn Reson Med* 1997;38(4):591–603.
48. Pruessmann KP, Weiger M, Scheidegger MB, Boesiger P. SENSE: sensitivity encoding for fast MRI. *Magn Reson Med* 1999;42(5):952–962.
49. Ibrahim TS, Mitchell C, Schmalbrock P, Lee R, Chakeres DW. Electromagnetic perspective on the operation of RF coils at 1.5–11.7 tesla. *Magn Reson Med* 2005;54(3):683–690.
50. Kumar A, Welti D, Ernst R. NMR Fourier zeugmatography. *J Magn Reson* 1975;18:69–83.
51. Edelstein WA, Hutchison JM, Johnson G, Redpath T. Spin warp NMR imaging and applications to human whole-body imaging. *Phys Med Biol* 1980;25(4):751–756.
52. Elster A, Burdette J. Questions and answers in magnetic resonance imaging. St Louis, Mo: Mosby-Year Book, 2001.
53. Bloch F, Hansen W, Packard M. The nuclear induction experiment. *Phys Rev* 1946;70:474–485.
54. Bloch F. Nuclear induction. *Phys Rev* 1946;70: 460–474.
55. Frahm J, Haase A, Matthaei D. Rapid three-dimensional MR imaging using the FLASH technique. *J Comput Assist Tomogr* 1986;10(2): 363–368.
56. Higgins DM. *ReviseMRI.com*. Available at: <http://www.reviseMRI.com>.
57. Twieg DB. The k-trajectory formulation of the NMR imaging process with applications in analysis and synthesis of imaging methods. *Med Phys* 1983;10(5):610–621.
58. Hennig J. K-space sampling strategies. *Eur Radiol* 1999;9(6):1020–1031.
59. Glockner JF, Hu HH, Stanley DW, Angelos L, King K. Parallel MR imaging: a user's guide. *RadioGraphics* 2005;25(5):1279–1297.
60. Hutchinson M, Raff U. Fast MRI data acquisition using multiple detectors. *Magn Reson Med* 1988;6(1):87–91.
61. Kwiat D, Einav S, Navon G. A decoupled coil detector array for fast image acquisition in magnetic resonance imaging. *Med Phys* 1991;18(2): 251–265.
62. Ra JB, Rim CY. Fast imaging using subencoding data sets from multiple detectors. *Magn Reson Med* 1993;30(1):142–145.
63. van den Brink JS, Watanabe Y, Kuhl CK, et al. Implications of SENSE MR in routine clinical practice. *Eur J Radiol* 2003;46(1):3–27.
64. Bammer R, Auer M, Keeling SL, et al. Diffusion tensor imaging using single-shot SENSE-EPI. *Magn Reson Med* 2002;48(1):128–136.
65. Hendrick RE, Nelson TR, Hendee WR. Optimizing tissue contrast in magnetic resonance imaging. *Magn Reson Imaging* 1984;2(3):193–204.
66. Lee JN, Riederer SJ. The contrast-to-noise in relaxation time, synthetic, and weighted-sum MR images. *Magn Reson Med* 1987;5(1):13–22.
67. Chenevert TL, McKeever PE, Ross BD. Monitoring early response of experimental brain tumors to therapy using diffusion magnetic resonance imaging. *Clin Cancer Res* 1997;3(9): 1457–1466.
68. Chenevert TL, Stegman LD, Taylor JM, et al. Diffusion magnetic resonance imaging: an early surrogate marker of therapeutic efficacy in brain tumors. *J Natl Cancer Inst* 2000;92(24):2029–2036.

69. Pomper MG, Port JD. New techniques in MR imaging of brain tumors. *Magn Reson Imaging Clin N Am* 2000;8(4):691–713.
70. Le Bihan D, Breton E, Lallemand D, Grenier P, Cabanis E, Laval Jeantet M. MR imaging of intravoxel incoherent motions: application to diffusion and perfusion in neurologic disorders. *Radiology* 1986;161:401–407.
71. Moseley ME, Kucharczyk J, Mintorovitch J, et al. Diffusion-weighted MR imaging of acute stroke: correlation with T2-weighted and magnetic susceptibility-enhanced MR imaging in cats. *AJNR Am J Neuroradiol* 1990;11(3):423–429.
72. Warach S, Chien D, Li W, Ronthal M, Edelman RR. Fast magnetic resonance diffusion-weighted imaging of acute human stroke. *Neurology* 1992;42:1717–1723.
73. Kidwell CS, Saver JL, Mattiello J, et al. Thrombolytic reversal of acute human cerebral ischemic injury shown by diffusion/perfusion magnetic resonance imaging. *Ann Neurol* 2000;47(4):462–469.
74. Rivers CS, Wardlaw JM, Armitage PA, et al. Do acute diffusion- and perfusion-weighted MRI lesions identify final infarct volume in ischemic stroke? *Stroke* 2006;37(1):98–104.
75. Restrepo L, Jacobs MA, Barker PB, et al. Etiology of perfusion-diffusion magnetic resonance imaging mismatch patterns. *J Neuroimaging* 2005;15(3):254–260.
76. Sorensen AG, Buonanno FS, Gonzalez RG, et al. Hyperacute stroke: evaluation with combined multisection diffusion-weighted and hemodynamically weighted echo-planar MR imaging. *Radiology* 1996;199(2):391–401.
77. Neumann-Haefelin T, Wittsack HJ, Wenserski F, et al. Diffusion- and perfusion-weighted MRI: the DWI/PWI mismatch region in acute stroke. *Stroke* 1999;30(8):1591–1597.
78. Kidwell CS, Alger JR, Saver JL. Beyond mismatch: evolving paradigms in imaging the ischemic penumbra with multimodal magnetic resonance imaging. *Stroke* 2003;34(11):2729–2735.
79. Kamel IR, Bluemke DA, Eng J, et al. The role of functional MR imaging in the assessment of tumor response after chemoembolization in patients with hepatocellular carcinoma. *J Vasc Interv Radiol* 2006;17(3):505–512.
80. Liapi E, Kamel IR, Bluemke DA, Jacobs MA, Kim HS. Assessment of response of uterine fibroids and myometrium to embolization using diffusion-weighted echoplanar MR imaging. *J Comput Assist Tomogr* 2005;29(1):83–86.
81. Jacobs MA, Herskovits EH, Kim HS. Uterine fibroids: diffusion-weighted MR imaging for monitoring therapy with focused ultrasound surgery—preliminary study. *Radiology* 2005;236(1):196–203.
82. Guo Y, Cai YQ, Cai ZL, et al. Differentiation of clinically benign and malignant breast lesions using diffusion-weighted imaging. *J Magn Reson Imaging* 2002;16(2):172–178.
83. Duyn JH, Gillen J, Sobering G, van Zijl PC, Moonen CT. Multisection proton MR spectroscopic imaging of the brain. *Radiology* 1993;188(1):277–282.
84. Henriksen O. In vivo quantitation of metabolite concentrations in the brain by means of proton MRS. *NMR Biomed* 1995;8(4):139–148.
85. Barker PB, Glickson JD, Bryan RN. In vivo magnetic resonance spectroscopy of human brain tumors. *Top Magn Reson Imaging* 1993;5(1):32–45.
86. Yeung DK, Cheung HS, Tse GM. Human breast lesions: characterization with contrast-enhanced in vivo proton MR spectroscopy—initial results. *Radiology* 2001;220(1):40–46.
87. Meisamy S, Bolan PJ, Baker EH, et al. Neoadjuvant chemotherapy of locally advanced breast cancer: predicting response with in vivo  $^1\text{H}$  MR spectroscopy—a pilot study at 4 T. *Radiology* 2004;233(2):424–431.
88. Kurhanewicz J, Vigneron DB, Nelson SJ, et al. Citrate as an in vivo marker to discriminate prostate cancer from benign prostatic hyperplasia and normal prostate peripheral zone: detection via localized proton spectroscopy. *Urology* 1995;45(3):459–466.
89. Glunde K, Jacobs MA, Bhujwala ZM. Choline metabolism in cancer: implications for diagnosis and therapy. *Expert Rev Mol Diagn* 2006;6(6):821–829.
90. Winter PM, Bansal N. TmDOTP $^{5-}$  as a  $^{23}\text{Na}$  shift reagent for the subcutaneously implanted 9L gliosarcoma in rats. *Magn Reson Med* 2001;45(3):436–442.
91. Winter PM, Bansal N. Triple-quantum-filtered  $^{23}\text{Na}$  NMR spectroscopy of subcutaneously implanted 9L gliosarcoma in the rat in the presence of TmDOTP $^{5-}$ . *J Magn Reson* 2001;152(1):70–78.
92. Perman WH, Thomasson DM, Bernstein MA, Turski PA. Multiple short-echo (2.5-ms) quantitation of in vivo sodium T2 relaxation. *Magn Reson Med* 1989;9(2):153–160.
93. Thulborn KR, Gindin TS, Davis D, Erb P. Comprehensive MR imaging protocol for stroke management: tissue sodium concentration as a



- measure of tissue viability in nonhuman primate studies and in clinical studies. *Radiology* 1999; 213(1):156–166.
94. Ouwerkerk R, Jacobs MA, Bottomley PA, Fajardo LL. A method for quantifying tissue sodium in breast tumors with short echo time  $^{23}\text{Na}$  MRI [abstr]. In: Proceedings of the 10th Meeting of the International Society for Magnetic Resonance in Medicine. Berkeley, Calif: International Society for Magnetic Resonance in Medicine, 2002; 2060.
  95. Jacobs MA, Ouwerkerk R, Wolff AC, et al. Multiparametric and multinuclear magnetic resonance imaging of human breast cancer: current applications. *Technol Cancer Res Treat* 2004; 3(6):543–550.
  96. Schepkin VD, Ross BD, Chenevert TL, et al. Sodium magnetic resonance imaging of chemotherapeutic response in a rat glioma. *Magn Reson Med* 2005;53(1):85–92.
  97. Schepkin VD, Lee KC, Kuszpit K, et al. Proton and sodium MRI assessment of emerging tumor chemotherapeutic resistance. *NMR Biomed* 2006;19(8):1035–1042.
  98. Ouwerkerk R, Jacobs MA, Macura KJ, et al. Elevated tissue sodium concentration in malignant breast lesions detected with non-invasive ( $^{23}\text{Na}$ ) MRI. *Breast Cancer Res Treat* 2007 Jan 27; [Epub ahead of print].
  99. Ouwerkerk R, Bleich KB, Gillen JS, Pomper MG, Bottomley PA. Tissue sodium concentration in human brain tumors as measured with  $^{23}\text{Na}$  MR imaging. *Radiology* 2003;227(2):529–537.
  100. Ouwerkerk R, Weiss RG, Bottomley PA. Measuring human cardiac tissue sodium concentrations using surface coils, adiabatic excitation, and twisted projection imaging with minimal T2 losses. *J Magn Reson Imaging* 2005;21(5):546–555.
  101. Maril N, Rosen Y, Reynolds GH, Ivanishev A, Ngo L, Lenkinski RE. Sodium MRI of the human kidney at 3 tesla. *Magn Reson Med* 2006; 56(6):1229–1234.
  102. Jacobs MA, Ouwerkerk R, Bottomley PA, Kim HS. Multiparametric proton and sodium MRI of uterine fibroids pre- and post-treatment [abstr]. In: Proceedings of the 13th Meeting of the International Society for Magnetic Resonance in Medicine. Berkeley, Calif: International Society for Magnetic Resonance in Medicine, 2005; 13.
  103. Jacobs MA, Ouwerkerk R, Bottomley PA, et al. Multiparameter proton, sodium, and spectroscopic imaging of human breast cancer [abstr]. In: Proceedings of the 11th Meeting of the International Society for Magnetic Resonance in Medicine. Berkeley, Calif: International Society for Magnetic Resonance in Medicine, 2003.
  104. Rosner CH, Markiewicz WD. High-field superconducting tape magnet technology. *IEEE Trans Magn* 1992;28(1):782–786.
  105. Heussner RW, Nunes CB, Lee PJ, Larbaletier DC, Jablonski PD. Properties of niobium-titanium superconducting wires with Nb artificial pinning centers. *J Appl Phys* 1996;80(3):1640–1646.
  106. Rudziak MK, Seuntjens JM, Renaud CV, Wong T, Wong J. Development of Apc Nb-Ti composite conductors at Supercon, Inc. *IEEE Trans Appl Superconductivity* 1995;5(2):1709–1712.
  107. Kangarlu A, Baertlein BA, Lee R, et al. Dielectric resonance phenomena in ultra high field MRI. *J Comput Assist Tomogr* 1999;23(6):821–831.
  108. Ibrahim TS, Lee R, Abduljalil AM, Baertlein BA, Robitaille PM. Dielectric resonances and B(1) field inhomogeneity in UHFMRI: computational analysis and experimental findings. *Magn Reson Imaging* 2001;19(2):219–226.
  109. Chen CN, Sank VJ, Cohen SM, Hault DI. The field dependence of NMR imaging. I. Laboratory assessment of signal-to-noise ratio and power deposition. *Magn Reson Med* 1986;3(5):722–729.
  110. Ibrahim TS. A numerical analysis of radio-frequency power requirements in magnetic resonance imaging experiment. *IEEE Trans Microw Theory Tech* 2004;52(8):1999–2003.
  111. Ibrahim TS, Lee R, Baertlein BA, Abduljalil AM, Zhu H, Robitaille PM. Effect of RF coil excitation on field inhomogeneity at ultra high fields: a field optimized TEM resonator. *Magn Reson Imaging* 2001;19(10):1339–1347.
  112. Beck BL, Jenkins K, Caserta J, Padgett K, Fitzsimmons J, Blackband SJ. Observation of significant signal voids in images of large biological samples at 11.1 T. *Magn Reson Med* 2004; 51(6):1103–1107.
  113. Liu F, Beck BL, Xu B, Fitzsimmons JR, Blackband SJ, Crozier S. Numerical modeling of 11.1T MRI of a human head using a MoM/FDTD method. *Concepts Magn Reson B Magn Reson Eng* 2005;24B(1):28–38.

## MR Imaging: Brief Overview and Emerging Applications

*Michael A. Jacobs, PhD et al*

RadioGraphics 2007; 27:1213-1229 • Published online 10.1148/rg.274065115 • Content Codes: MR PH

---

### Page 1217

Localization of the MR signal is obtained by applying a gradient that produces a controlled linear spatial variation of the B0 magnetic field (z direction), which creates small perturbations to the field in three directions (x, y, and z) (Fig 1).

### Page 1220

The mechanism for contrast in an MR image is governed by the application of an RF pulse and, more important, the relaxation times of the tissue of interest, in particular T1 and T2. After the RF pulse, an MR signal is created.

### Page 1220

T1 weighting of the image is dependent on the amount of TR in milliseconds between the slice selection and RF pulses and the field strength.

### Page 1220

T2-weighted images are dependent on the amount of TE in milliseconds.

### Page 1224

The real power of MR imaging lies in the wide range of applications for which it can be used. Current applications include soft-tissue delineation, determining extent of disease, tumor staging, functional and metabolic information, and monitoring response to treatment.